New Multi-Tooth Inter-Modular Flux Reversal Permanent Magnet Motor

Mohammad Reza Sarshar[1)], Mohammad Amin Jalali Kondelaji[2)], Pedram Asef [2)], Mojtaba Mirsalim[1)]

1) Amirkabir University of Technology (Tehran Polytechnic), Department of Electrical Engineering, Tehran, Iran

E-mail: rezasarshar@aut.ac.ir, mirsalim@aut.ac.ir

2) University College London, Department of Mechanical Engineering, e-Motion Laboratory, London, United Kingdom

E-mail: amin.jalali@ucl.ac.uk, pedram.asef@ucl.ac.uk

ABSTRACT: This paper offers a new motor topology, multi-tooth inter-modular flux reversal permanent magnet (FRPM) motor, in which the PMs are positioned between the teeth of stator's wound pole (tooth PMs) and between the stator modules (inter-modular PMs). By using the motor's magnetic equivalent circuit, it is reported that the tooth PMs reduce the stator pole flux density while increasing the air-gap flux density. The motor specifications including dimensions are obtained by a multi-objective optimization using genetic algorithm. Two-dimensional finite element analysis is used to achieve the main operating characteristics in terms of flux density distributions, back-EMF, output torque, overload performance, and efficiency maps. Two benchmark inter-modular PM (IMPM) motors are studied as comparison criterion to highlight the achievements of the promising new motor topology. It is shown that the new structure improves the average torque by almost 45% compared to the benchmark IMPM while decreasing PM volume. Also, by examining the efficiency maps, the new motor topology indicates a 3.5 times larger high-efficiency area than its benchmark counterparts.

KEY WORDS: Finite element analysis, flux reversal permanent magnet motor, inter-modular structure, magnetic equivalent circuit.

1. INTRODUCTION

Rare-earth materials in electric motors, especially neodymium-iron-boron (NdFeB) permanent magnets (PMs), contribute to high torque production. The PMs can be positioned into either stationary or rotating part. The rotor-PM motors, including surface-mounted PM synchronous motors (PMSMs) and interior PM motors (IPMs) are used in several applications, such as electric vehicles (EVs). Rotor-PM motors benefit from high torque density and efficiency. However, these structures suffer from PM demagnetization risk due to the existence of high vibration and centrifugal forces on the PMs [(1)]. Additionally, due to losses, the PMs' temperature rises, which is not easy to apply the coolant in the rotating part. Therefore, stator-PM motors have gained attention in electric machine design for electric vehicles [(2), (3)].

Stator-PM motors can be classified into several groups according to PM arrangement or excitation type. PM-assisted switched reluctance motors (PMaSRM) benefit from a robust structure and are appropriate for high-speed applications. However, PMaSRMs suffer from low torque density, high torque ripples, and non-conventional drive circuits [(4)-(6)]. Other stator-PM topologies are divided by their PM arrangement. Biased-flux PM (BFPM) motors, in which PMs are arranged in the stator yoke (or slot-opening) to lower the stator pole flux and saturation risk [(7)]. Also, other synthesized structures, such as inter-modular PM (IMPM), are proposed to have a better PM heat dissipation than other stator-PM motors [(8)]. In BFPM-based topologies (such as IMPM), the PMs are tangentially magnetized to use the quasi-flux concentrating effect and boost the air gap flux density [(9)].

Flux-switching PM motors (FSPMs) benefit from the flux-concentrating effect, in which the armature coils sandwich the PMs, and the PMs are tangentially magnetized. This PM arrangement pushes the armature flux to the air gap and significantly reduces the leakage flux[(1)]. Furthermore, flux reversal PM motors (FRPM) comprise another category of stator-PM motors. In FRPMs, PMs are parked on the stator surface area and have four-quadrant energy conversion [(10)-(13)]. Much of the research conducted has also utilized combined PM arrays, taking advantage of the benefits of each configuration [(14)]. In [(15)], a dual-PM machine was introduced, in which the synergies of flux-switching (FS) and flux reversal (FR) effects were utilized. This synergistic PM array protects the motor from over-structuration.

In this study, a new inter-modular FRPM motor with multi-tooth topology is proposed, which employs the features of IMPM and FRPM motors. This combined PM configuration is mainly utilized to increase the torque production and decrease the torque ripple, which are essential factors for an electric vehicle. In section 2, the

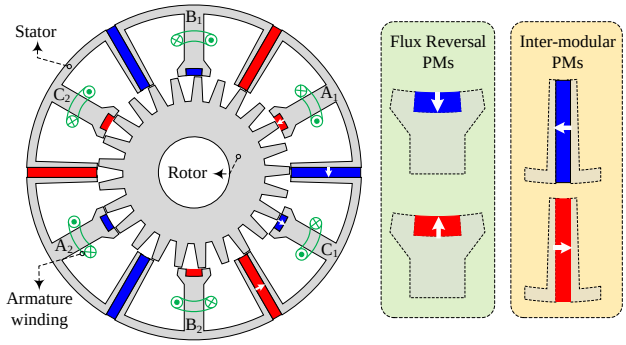

Fig. 1 The proposed modular E-shaped stator-PM motor.

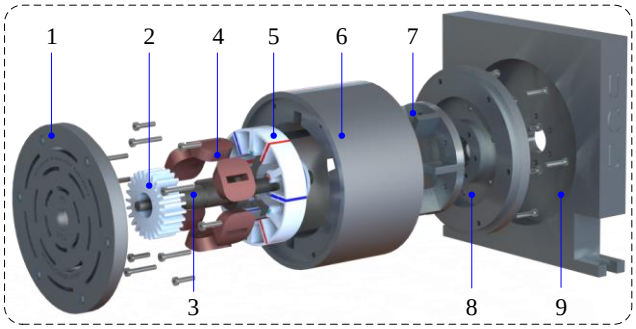

Fig. 2 The exploded view of the proposed motor. (1) End cap. (2) Rotor. (3) Shaft. (4) Coils. (5) Stator. (6) House shell. (7) Leveler. (8) End cap. (9) Stand.

proposed motor is introduced and the methodology of the idea behind it is illustrated with a simplified magnetic equivalent circuit. In section 3, the finite element analysis (FEA) is used to carry out the results under two conditions (no-load and full load) of the motor and the results are compared with those of the benchmark motors. Finally, a conclusion is given in section 4.

2. MOTOR STRUCTURES AND METHODOLOGY

2.1. Topology and Working Principles

As Fig. 1 depicts, the proposed motor contains two PM arrays: tooth PMs and inter-modular PMs. These two PM arrays offer two effects to the proposed motor: tooth PMs and inter-modular PMs have the flux reversal (FR) and biased-flux (BF) effects, respectively. The main goal of combining these two PM arrays is to boost the air-gap flux density while decreasing the stator pole flux density. Fig. 2 depicts the exploded view of the motor to indicate its manufacturability. Two benchmark motors are studied to highlight the advantages of the FR effect. Fig. 3a shows the benchmark 18/11-tooth inter-modular PM motor (IMPM) [8]. Additionally, Fig. 3b illustrates the multi-tooth 24/25-tooth IMPM. The basic design parameters of the motors are listed in Table 1. All main dimensions such as air-gap length, stack length, and stator diameter are equal to offer a fair comparison.

Table 1 Basic Design Parameters of motors.

Parameter	Proposed Motor	18/11 IMPM [8]	24/25 IMPM
Number of stator teeth	24	18	24
Number of rotor teeth	25	11	25
Frequency	166.67 Hz		
Speed	400 rpm	900 rpm	400 rpm
Stator outer radius	47 mm		
Stack length	20 mm		
Air-gap length	0.4 mm		
Current density	6 A/mm^2		
PM volume	8cm^3	12cm^3	6.5cm^3

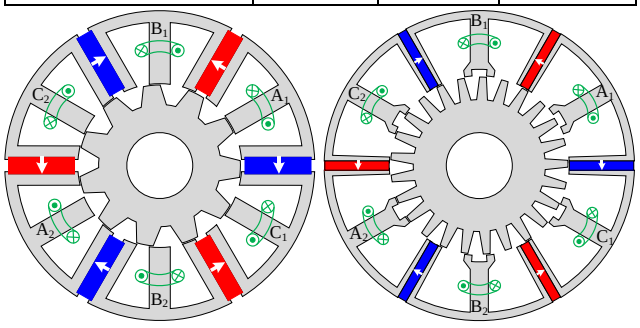

Fig. 3 Benchmark motors. (a) 18/11 IMPM [6] (b) 24/25 IMPM.

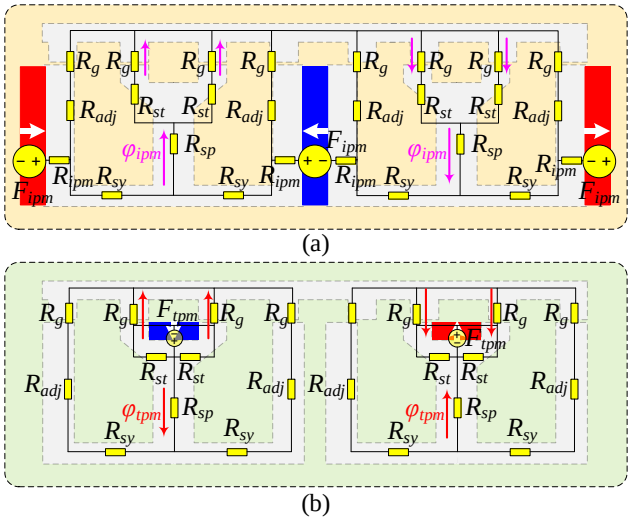

Fig. 4 Magnetic equivalent circuit for each PM array. (a) BF effect and (b) FR effect.

The contributions of these two PM arrays can be shown by applying a magnetic equivalent circuit (MEC), which is drawn in Fig. 4 for each PM arrangement; 1) with just inter-modular PMs (Fig. 4a) and 2) with just flux reversal PMs (Fig. 4b).

φ_{ipm} denotes the stator pole flux created by the inter-modular PMs and can be calculated as:

$$\varphi_{ipm} = \frac{F_{ipm}}{R_{ipm}+R_1} \times \frac{R_g+R_{adj}}{R_1+R_g+R_{adj}} \qquad (1)$$

where R_1 can be written as:

$$R_1 = (R_{sp} + R_{sy} + R_g + R_{st}) \parallel (R_g + R_{adj}) \qquad (2)$$

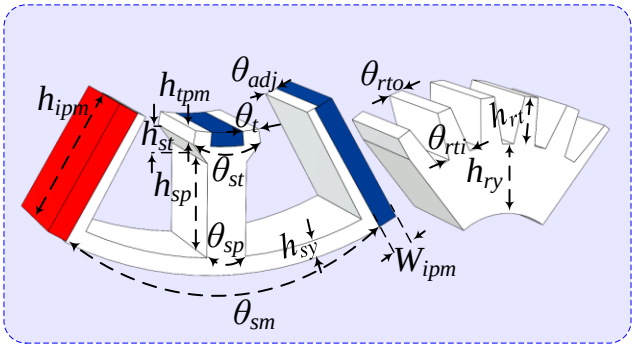

Fig. 5 Optimization parameters of the proposed structure.

Table 2 Optimized dimensions of the proposed motor.

Definition	Symbol	Value
Stator module arc angle (°)	θ_{sm}	28.2
Stator yoke height (mm)	h_{sy}	2.5
Stator pole angle (°)	θ_{sp}	3.5
Stator pole height (mm)	h_{sp}	13
Stator pole outer angle (°)	θ_{st}	9.3
Stator teeth height (mm)	h_{st}	2.4
Tooth PM height (mm)	h_{tpm}	2
Stator teeth angle (°)	θ_t	4.7
Stator adjacent pole outer angle (°)	θ_{adj}	2.5
Inter-modular PM height (mm)	h_{ipm}	19.5
Inter-modular PM width (mm)	W_{ipm}	2.8
Rotor yoke height (mm)	h_{ry}	10
Rotor teeth height (mm)	h_{rt}	6.8
Rotor teeth outer arc angle (°)	θ_{rto}	4.4
Rotor teeth inner arc angle (°)	θ_{rti}	9.4

Also, φ_{tpm} denotes the stator pole flux caused by just flux reversal PMs (tooth PMs) and is written as:

$$\varphi_{tpm} = \frac{F_{tpm}}{\frac{1}{2}\times(2R_g+R_{adj}+R_{sy})+R_{sp}} \qquad (3)$$

The superposition of φ_{ipm} and φ_{tpm} results in the final stator pole for the proposed structure (φ_{sp}) and, by considering the direction of each flux, it can be calculated as:

$$\varphi_{sp} = \varphi_{ipm} - \underbrace{\varphi_{tpm}}_{\text{FReffect}} \qquad (4)$$

Eqn. (4) confirms that the FR effect improves the saturation risk of the stator pole and prepares the motor for better overload performance by reducing φ_{sp}.

Furthermore, the air-gap flux density is increased thanks to the FR effect and can be validated using MEC. φ_{ag} shows the air-gap flux density and φ_{ag-ipm} and φ_{ag-tpm}, demonstrating the air-gap flux density resulting from inter-modular and flux reversal PMs, respectively. φ_{ag} can be developed as:

$$\varphi_{ag} = \varphi_{ag-ipm} + \underbrace{\varphi_{ag-tpm}}_{\text{FReffect}} \qquad (5)$$

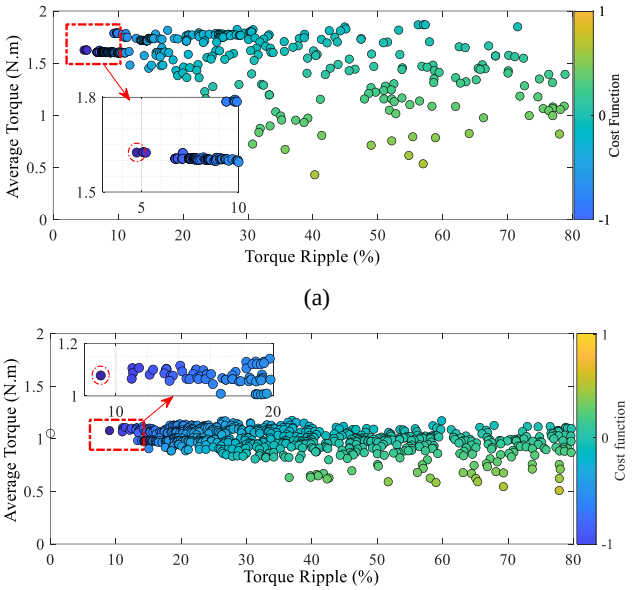

(a)

(b)

Fig. 6 Optimization process for (a) proposed motor and (b) 24-25 IMPM structure.

The direction of each PM array causes this increase in the air-gap flux density, as shown in Fig. 4 and eqn. (6) calculates each PM array's air-gap flux density. This improvement can be seen in the torque production increase for the proposed motor.

$$\begin{cases} \varphi_{ag-ipm} = \frac{\varphi_{ipm}}{2} \\ \varphi_{ag-tpm} = \frac{F_{tpm}}{R_{st}+2R_g} \end{cases} \qquad (6)$$

2.2. Genetic Algorithm Optimization

Genetic algorithm (GA) optimization is applied to the motor parameters, as shown in Fig. 5, to acquire the optimized sizing of the proposed structure. The cost function (*CF*) of the optimization process is expressed in (7).

$$CF = 1.1 - \left(0.85 \times \frac{T_{avg}}{T_{avg,desired}} + 0.15 \times \frac{T_{rip,desired}}{T_{rip}}\right) \qquad (7)$$

where T_{avg} and T_{rip} show the average torque and torque ripple, respectively. Also, according to the motor structure and volume, desired average torque and ripple, which are denoted by $T_{avg,desired}$ and $T_{rip,desired}$, are set at 1.5Nm and 5%, respectively. The optimization process for the proposed motor and 24/25 pole IMPM are shown in Figs. 6a and 6b, respectively. Each point shows each sample's average torque and ripple. The Pareto front for the proposed motor shows that the optimized proposed motor performs at 1.6Nm torque with a lower than 5% ripple. The torque profile peformance for the proposed motor shows 45% improvement in average torque compared to 24/25 IMPM. By

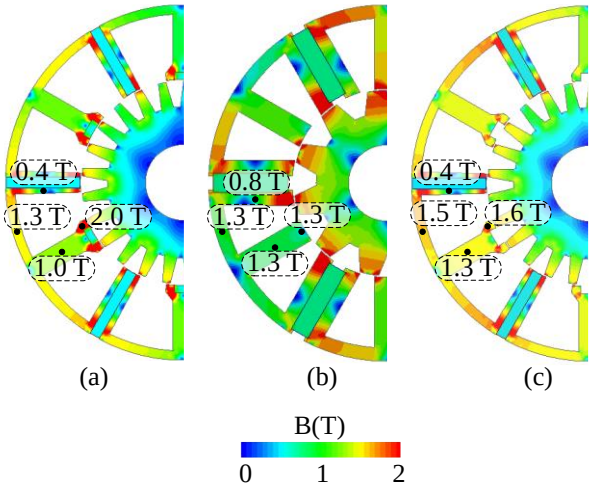

Fig. 7 Open-circuit flux density distributions of (a) the proposed motor, (b) 18/11 IMPM, and (c) 24-25 multi-tooth IMPM.

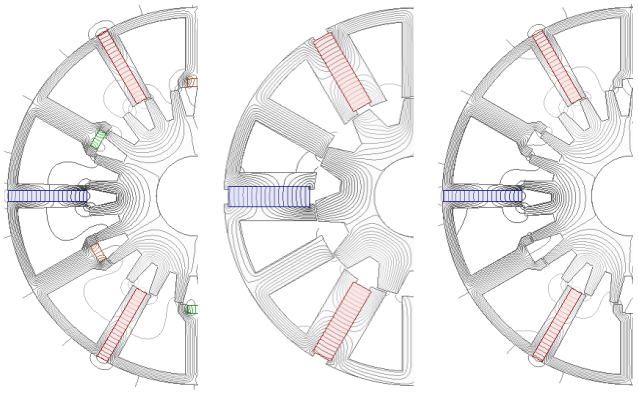

Fig. 8 Open-circuit flux line distributions of (a) the proposed motor, (b) 18/11 IMPM, and (c) 24-25 multi-tooth IMPM.

coupling the finite element Software and GA, over 1000 samples are examined, and the optimized parameter values of the motor are listed in Table 2. Also, 18/11 IMPM was optimized by genetic algorithm in [8], and has 1.1Nm average torque with 5.1% ripple.

3. RESULTS AND DISCUSSIONS

We conduct our studies under two conditions: 1) No-load condition and 2) steady-state full-load condition.

3.1. No-Load Condition

The flux density distributions of the three motors are illustrated in Fig. 7 to show the impact of each PM array. Also, the average magnitudes of flux densities for four points in the stator are shown in Fig. 6. No global saturation area is witnessed in the three motors. As shown, the FR effect decreases the stator pole flux density by 23% compared to the IMPM motors and lowers the saturation risk. Also, the other advantage of the FR effect is boosting the air-gap

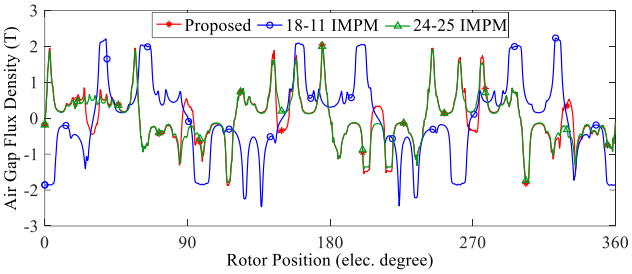

Fig. 9 Comparison of no-load air gap flux density profiles.

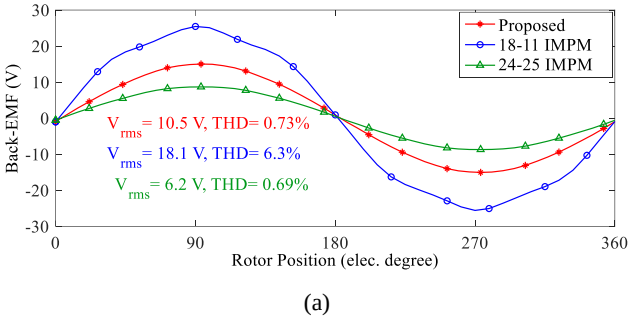

(a)

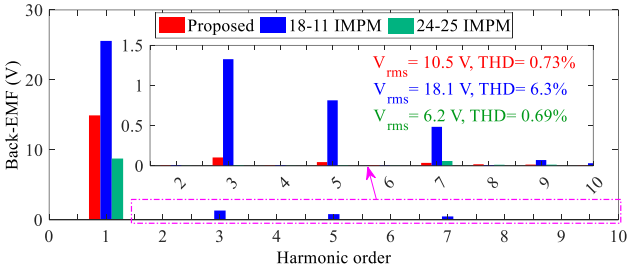

(b)

Fig. 10 Comparison of (a) back-EMF profiles and (b) harmonic distribution.

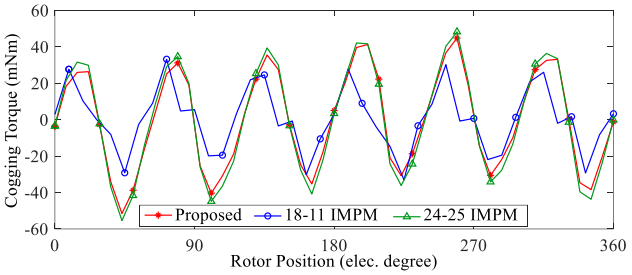

Fig. 11 Comparison of cogging torque profiles.

flux density, which is improved by 53% and 25% compared to 18/11 and 24/25 IMPMs, respectively. The FEA validates the analytical results obtained in the previous section. Moreover, Fig. 8 shows the flux lines of the motors in no-load conditions. It shows that the leakage flux of all three motors is low. No-load air-gap flux density waveforms of the motors are drawn in Fig. 9. In most rotor positions, the proposed motor and 24/25 IMPM have the same value (due to structure similarity), but in several points, the proposed motor has higher flux density, which highlights the effect of tooth PMs (FR effect).

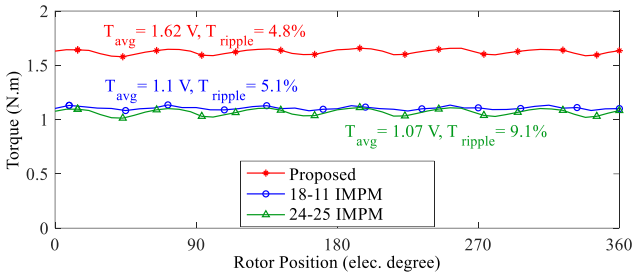

Fig. 15 Comparison of torque profiles.

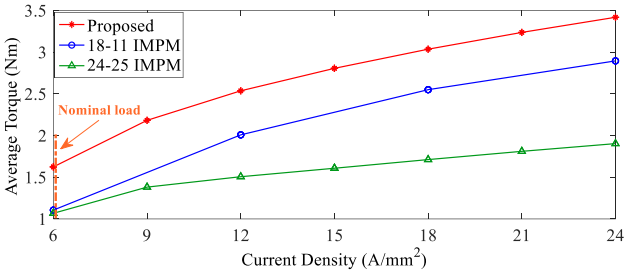

Fig. 16 Comparison of overload torque profiles.

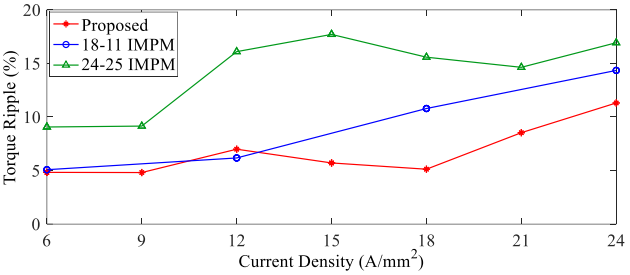

Fig. 17 Comparison of overload torque ripple profiles.

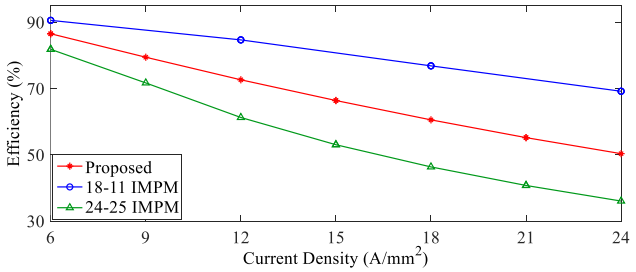

Fig. 19 Comparison of overload efficiencies.

Figs. 10a and 10b exhibits the back-electro-motive force (back-EMF) curves and space harmonic distribution of the motors, respectively. The proposed motor generates a 10.3 V RMS back-EMF with 0.7% total harmonic distortion (THD), which is suitable for its regenerative mode. However, the 18/11 IMPM produces 7.6 V higher back-EMF waveform, but it suffers from a high 6.3% THD,

which is 8.6 times higher than the proposed motor. Moreover, the motors' cogging torque profiles are shown in Fig. 11. The motors show an acceptable and low peak-to-peak (pk2pk) value of cogging torque (lower than 0.1 Nm) and have similar performance.

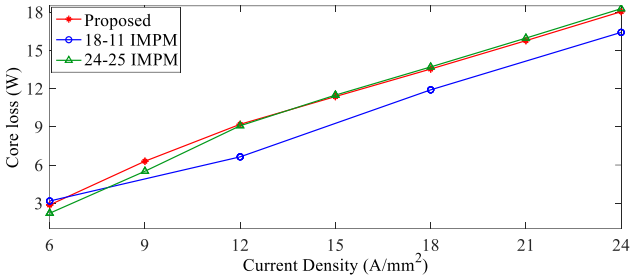

Fig. 18 Comparison of overload core loss.

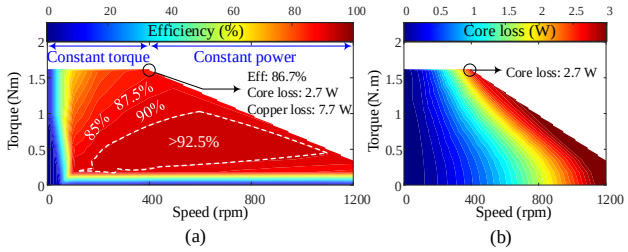

Fig. 19 (a) Efficiency and (b) core loss maps for the proposed motor.

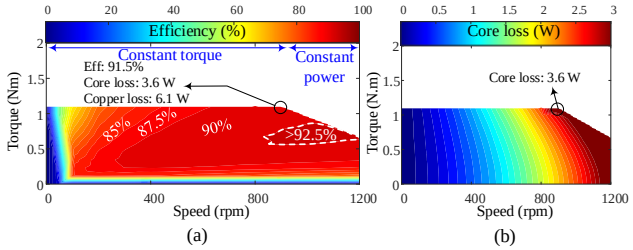

Fig. 20 (a) Efficiency and (b) core loss maps for 18/11 IMPM.

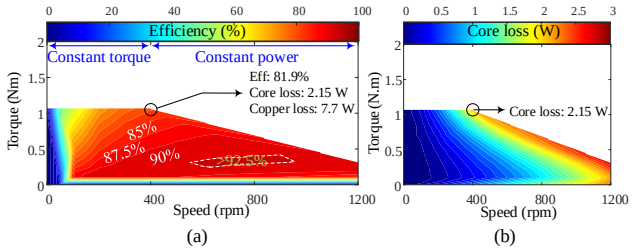

Fig. 21 (a) Efficiency and (b) core loss maps for 24/25 IMPM.

3.2. Full-Load Condition

The full-load condition is obtained when the armature winding is excited by current density of 6 A/mm^2 which is selected for better thermal management. The steady-state torque profiles of the motors are demonstrated in Fig. 15. The proposed motor has increased the output torque by 47%

compared to 18/11 IMPM while decreasing the PM volume by 46%. The FR effect (tooth PMs) has also improved the 24/25 IMPM torque by 48%. In the case of torque ripple percentage, the proposed structure has decreased the torque ripple compared to the 18/11 and 24/25 IMPMs by 5.8% and 47%, respectively. The overload performances (until four times higher than the nominal load) of the motors are investigated. Fig. 11 presents the motors'

average overload torque, showing that the proposed motor has improved by at least 45% compared to the other two benchmark motors across all current densities. The upward trend and slope exhibited by 18/11 IMPM and the proposed motor are greater than 24/25 IMPM, which could be related to its saturation. Additionally, in terms of torque ripples during overload conditions, the proposed motor demonstrates the lowest ripple across the most of current densities (Fig. 17). By examining these two factors (average torque and ripple), it indicates that the proposed motor performs promising and safe under overload conditions. By comparing efficiency under overload conditions, even up to four times the nominal condition, which is shown in Fig.19, the efficiency of the proposed motor and 18/11 IMPM motor remains above 50%. In overload conditions, the proposed motor exhibits a core loss of 18W at a current density excitation of 24 A/mm², which is the same as the 24/25 IMPM. The 18/11 IMPM achieves 2.25 times higher speed than the 24/25 IMPM and the proposed motor, due to its rotor teeth count, while maintaining the same frequency. However, since output power is directly related to speed and torque, the 18/11 IMPM delivers higher output power compared to the proposed structure and 24/25 IMPM. The efficiency and core loss maps for the motors are drawn in Figs. 19 to 21, to investigate the efficiency and core loss of the motors in different loads and speeds. In the range of 0 to 1200 rpm, the proposed motor achieves an efficiency above 92.5%, with an area 3.5 times larger than that of the other motors. This demonstrates that, in scenarios where speed remains constant and torque is the primary factor influencing output power, the proposed motor delivers markedly enhanced performance. Additionally, for the proposed motor, approximately 70% of the efficiency map area exhibits an efficiency greater than 90%.

For the inter-modular PMs, three points were selected in different regions. By analyzing the flux density at these points and knowing the demagnetization limit of the NdFeB-N42 PM at 80°C, which is 0.1 Tesla, it is observed that none of the points experience demagnetization. This analysis is also conducted for the tooth PMs, and it was found that this PMs also maintain a safe margin from the demagnetization limit. Based on Fig. 23, it is noteworthy that the 18/11 IMPM motor, due to having approximately double the PM volume, also exhibits a flux density that is approximately double. Table 3 compares the performance of the proposed motor, 18/11 IMPM, and 24/25 IMPM, highlighting the proposed motor improvements. The proposed motor offers a higher average torque (1.62 Nm) and lower torque ripple (4.8%) than the 18/11 IMPM

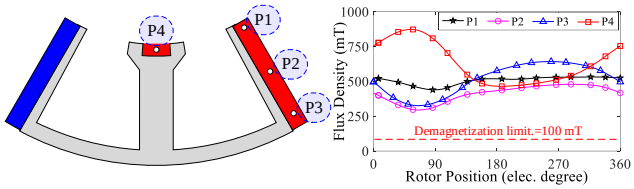

(a) (b)

Fig. 22 Demagnetization curves. (a) Points. (b) Flux density curves.

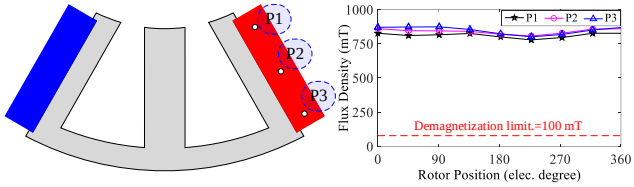

(a) (b)

Fig. 23 Demagnetization curves. (a) Points. (b) Flux density curves.

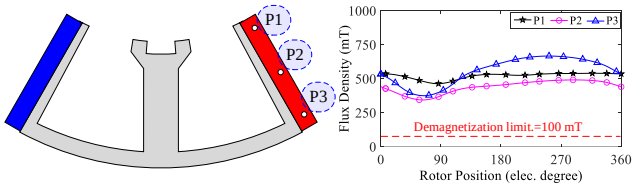

(a) (b)

Fig. 24 Demagnetization curves at 80°C. (a) Points. (b) Flux density curves.

Table 3 Comparison of Motors' Performances.

Parameter	Proposed Motor	18/11 IMPM [6]	24/25 IMPM
Average torque (Nm)	1.62	1.1	1.07
Torque ripple (%)	4.8	5.1	9.1
Efficiency (%)	86.7	91.5	81.9
Core loss (W)	2.7	2.15	3.6
Copper loss (W)	7.7	7.7	6.1
PM torque volume (Nm/L)	**202**	91	164
Output power (W)	67.85	103.62	44.8

(1.1 Nm, 5.1%) and 24/25 IMPM (1.07 Nm, 9.1%), with an efficiency of 86.7%. The proposed motor also shows reduced core loss (2.7 W) and copper loss (7.7 W), and a significantly higher PM torque volume (202 Nm/L) compared to 91 and 164 Nm/L for the other motors, respectively. The proposed motor boosts PM torque density by 122% and 23% over the 18/11 and 24/25 IMPM, respectively. With an output power of 67.85W, the proposed motor demonstrates an overall enhanced performance.

4. CONCLUSIONS

This paper presented a new stator-PM motor with a dual-PM array benefiting biased-flux (BF) and flux reversal (FR) effects.

Adding FR to the inter-modular PM (IMPM) structure lowered the saturation risk and enhanced the air-gap flux density, as shown by conducting a two-step magnetic equivalent circuit. Additionally, for a fair comparison, all three motors were optimized using a genetic algorithm to achieve the maximum torque with the minimum ripple, and their cost functions were thoroughly analyzed. Also, finite element analysis (FEA) studies for no-load conditions verified the analytical results and showed a 23% decrease in stator pole flux density. The back-EMF THD improved by 88% compared to 18/11 IMPM, and the full-load simulations proved a 47% enhancement in the output torque. In overload conditions, the proposed motor also exhibited superior performance in terms of average torque, maintaining higher torque across all current densities and loads compared to the other motors. Furthermore, in most load conditions, the proposed motor demonstrated the lowest torque ripple among the motors. Finally, upon analyzing the efficiency maps of the motors, the proposed motor showed a range with efficiency above 92.5%, covering an area 3.5 times larger than that of the other IMPM motors, highlighting the impact of the flux reversal (FR) and tooth magnets. Furthermore, none of the points in any of the motors experienced demagnetization, ensuring the reliable performance of the motors.

REFERENCES

(1) Y. Bi, W. Fu, S. Niu, X. Zhao, J. Huang, and Z. Qiao, “Torque enhancement of a dual-pm flux-switching machine with improved multiple high-order working harmonics,” IEEE Transactions on Transportation Electrification, vol. 10, no. 2, pp. 2830–2843, 2024.

(2) T. Jiang, W. Zhao, and L. Xu, “Analysis of split-tooth stator-pm vernier machines with zero-sequence current excitation,” IEEE Transactions on Industrial Electronics, vol. 70, no. 2, pp. 1229–1238, 2023.

(3) Kondelaji, M. A. J., Farahani, E. F., & Mirsalim, M. (2020). Performance analysis of a new switched reluctance motor with two sets of embedded permanent magnets. IEEE Transactions on Energy Conversion, 35(2), 818-827.

(4) Farahani, E.F., Kondelaji, M.A.J., Mirsalim, M.: ‘An innovative hybrid-excited multi-tooth switched reluctance motor for torque enhancement’, IEEE Transactions on Industrial Electronics, 2020, 68, (2), pp. 982–992

(5) Y. Hasegawa, K. Nakamura, and O. Ichinokura, “A novel switched reluctance motor with the auxiliary windings and permanent magnets,” IEEE transactions on magnetics, vol. 48, no. 11, pp. 3855–3858, 2012.

(6) M. A. J. Kondelaji and M. Mirsalim, "Segmented-Rotor Modular Switched Reluctance Motor With High Torque and Low Torque Ripple," in IEEE Transactions on Transportation Electrification, vol. 6, no. 1, pp. 62-72, March 2020, doi: 10.1109/TTE.2020.2969356.

(7) M. Amirkhani, M. A. J. Kondelaji, A. Ghaffarpour, M. Mirsalim, and S. Vaez-Zadeh, “Study of boosted toothed biased flux permanent magnet motors,” IEEE Transactions on Transportation Electrification, vol. 8, no. 2, pp. 2549–2564, 2022.

(8) M. Amirkhani, E. F. Farahani, and M. Mirsalim, “Study of an improved biased flux intermodular permanent magnet motor, IEEE Transactions on Transportation Electrification, pp. 1‑1, 2023.

(9) E. F. Farahani, M. Amirkhani, A. Khorsandi, N. J. Baker and M. Mirsalim, "Split Yoke-Permanent Magnet Biased-Flux Motor," in IEEE Transactions on Energy Conversion, doi: 10.1109/TEC.2024.3474920.

(10) F. Wei, Z. Q. Zhu, X. Sun, L. Yan and J. Qi, "Investigation of Asymmetric Consequent-Pole Hybrid Excited Flux Reversal Machines," in IEEE Transactions on Industry Applications, vol. 58, no. 3, pp. 3434-3446, May-June 2022.

(11) M. R. Sarshar, M. A. Jalali Kondelaji, and M. Mirsalim, “Study of an improved flux reversal permanent magnet outer-rotor motor,” in 2024 32nd International Conference on Electrical Engineering (ICEE), 2024, pp. 1–4.

(12) H. Yang, Z. Q. Zhu, H. Lin, H. Li, and S. Lyu, “Analysis of consequent-pole flux reversal permanent magnet machine with biased flux modulation theory,” IEEE Transactions on Industrial Electronics, vol. 67, no. 3, pp. 2107–2121, 2020.

(13) Sarshar, M.R., Kondelaji, M.A.J., Mirsalim, M. Analysis of a synthesized slot permanent magnet flux reversal motor. In: 2023 3rd International Conference on Electrical Machines and Drives (ICEMD), 2023. pp. 1‑4

(14) F. Wei, Z. Q. Zhu, L. Yan and J. Qi, "Investigation of Stator/Rotor Pole Number Combinations and PM Numbers in Consequent-Pole Hybrid Excited Flux Reversal Machine," in IEEE Transactions on Energy Conversion, vol. 37, no. 3, pp. 2092-2106, Sept. 2022, doi: 10.1109/TEC.2022.3163654.

(15) S. Cai, H. Chen, X. Yuan, Y.-C. Wang, J.-X. Shen, and C. H. T. Lee, “Analysis of synergistic stator permanent magnet machine with the synergies of flux-switching and flux-reversal effects,” IEEE Transactions on Industrial Electronics, vol. 69, no. 12, pp. 12237–12248, 2022.